KLOE Note N. 165
October 1997

Parameterization of the time to distance relations and of the resolution functions for Prototype 1

M. Primavera, S. Spagnolo
I.N.F.N., Sezione di Lecce

Abstract

The full length prototype of the KLOE drift chamber, has been exposed, at CERN, to a 50 Gev/c π beam. Results on time to distance relations (as functions of the different parameters involved) and on cell resolution functions are presented and discussed.

1 Introduction

Prototype 1 (see fig. 1) has been widely described [1], [2], [3], [4], [5]. It was firstly monitored under cosmic rays, and then exposed to a beam at CERN, in order to analyse its performances in different configurations and to obtain the detector calibration constants: t_0, time to distance relations, resolution functions, efficiencies, wire offsets from nominal positions, signal transit time, etc.

The cell response in Prototype 1, as in the KLOE final chamber, depends, besides of the external running conditions (wire voltages, gas composition, temperature and pressure), also on the track orientation, in the cell reference frame, and on the cell shape, which determines the configuration of the electric field at the edges of the cell. The final aim of time to distance relation and resolution analysis is to describe as accurately as possible the cell behaviour, containing as much as possible the number of the required parameters. To this purpose, GARFIELD [6] simulations, confirmed by the data, showed that the fundamental parameters which condition the cell response are: the angles ϕ at which the track crosses the cell with respect to the wire reference frame described in ref. [8] (see Fig. 1), and the cell deformation along z. Due to the stereo geometry, the outer part of each cell changes its shape along z and this deformation, which manifests itself at the cell corners, is periodic along z and can be parametrized by the β_u angle shown in Fig. 1. Moreover, wire displacements from their nominal positions, coming from tolerances on the wire positions at the chamber end plates and bad wire tensioning will affect the x-t relations and the resolutions inside the cell.

In this note, we present a description of the different data samples used for the comprehensive analysis of the x-t relations and of the resolution functions, together with the procedures followed to obtain them. The dependence on external factors like gas pressure P and temperature T has not been studied here, because the data didn't contain significative differences in P and T for runs collected in the same conditions.

2 The Prototype 1 beam test

In may-june 1995 Prototype 1 has been exposed to the SPS T1-X7 beam in the West Area at CERN. In fig. 2 the schematic layout of the experimental setup is shown.

The beam consisted of 50 GeV/c momentum particles, 90% π^+ and 10% e^+. The beam profile was asymmetric and could be described by two gaussians: the first one with $\sigma = 1.5\ cm$ and the second one with $\sigma = 2.5\ cm$, respectively in the vertical and horizontal directions (y and z in fig. 2). The maximum number of particles was of $1.3 \cdot 10^3$ during 2.4 s of spill time, over the total SPS working cycle of 14.4 s.

Two pairs of scintillation counters, one placed upstream and the other downstream of Prototype 1, were used for trigger in a quadruple delayed coincidence. The time jitter of the trigger was estimated to be of the order of 1-2 ns. For each pair the useful overlapping region was $5. \times 5.\ cm^2$ or, $12. \times 12.\ cm^2$ for a totally defocused beam.

An optical system, consisting on a He-Ne red laser, mirrors and positioning stage, was used to align the beam at the required directions with respect to the prototype frame.

A motor system allowed to translate Prototype 1 along the y and the z axis in fig. 2 and to rotate it around them, in order to select all possible orientations of the beam with respect to the chamber, respectively, for the polar and the azimuthal angles.

The gas mixture was set to 90% of helium and 10% of isobutane by means of mass flowmeters and the gas flow was monitored by electronic mass flow controllers. Gas pressure, temperature and humidity were also registered.

The high voltage on wires was set by a remotely controlled high voltage system. Different runs, with different voltages on sense and guard wires were taken. However, for the analysis described in this note, data collected at 1950 V on sense wires of 3×3 cells, at 1750 V on sense wires of 1.5×1.5 cells and at 700 V on guard wires.

The front-end electronics consisted of the Tektronix VTX preamplifier cards and the KLOE postamplifier-discriminator circuits. The equivalent discriminator thresholds were changed from 2 to 6 mV during the data taking, in order to study noise effects, but the data referred in this note were collected with a threshold of 4 mV.

The drift times were acquired with TDC LeCroy 2277 (for a total number of 480 readout channels), while 74 of the innermost cells were also equipped, for charge measurements, with ADC LeCroy 2249W and CAEN C205A.

A more detailed description of the beam test setup can be found in ref. [5], which reports the whole data analysis, including results about noise, efficiency, chamber gas monitoring, gain studies, energy loss resolution, angular resolution, etc.

3 The data samples

In order to performe a complete and systematic study of the chamber performances with respect to the relevant working parameters involved, many sets of "dedicated" runs were acquired, for a total number of 27×10^6 events written on tape. As far as space to time relations and resolutions are concerned, data were taken in such a way to illuminate the whole cell, at different positions along z and with tracks at different orientations with respect to the sense wire. In detail, 4 sets of runs were used:

- "y scanning", performed by translating the chamber along the y axis in a range of $\Delta y = \pm 26$ cm in step of 2 cm around the so called "canonical position". In the "canonical position" of Prototype 1 the beam crossed the chamber radially at z=0, in the middle of the cylindrical sector, as shown in Fig. 2. This scanning allowed to illuminate the most of the cells.

- "ϕ scanning", performed in the $z = 0$ plane by rotating around the z axis (ϕ angle) and translating in y Prototype 1, in order to study the cell behaviour as a function of ϕ.

- "z scanning", performed by translating the chamber along the z axis of ± 120 cm in step of 30 cm (coarse z scanning) and of ± 14 cm in step of 2 cm (fine z scanning). In this scanning the beam crossed the chamber radially at different transverse positions. The fine z scanning covers more than one period of β_u variation for all the cells in the three different Prototype 1 regions, while the coarse z scanning covers a large part of the chamber length.

- "θ scanning", performed by rotating around the x axis (θ angle) and translating in z Prototype 1. In this scanning the beam direction has a component along the chamber longitudinal axis, allowing for studies of the gravitational sagitta effects and dE/dx as a function of the sampled track length.

4 The parameterization of the cell response

4.1 Motivations for unhomogeneous cell behaviours

One of the main motivations for building Prototype 1 was the possibility of studying the cell response in the real environment of the KLOE tracking detector, in order to reproduce closely all its peculiar features. The need for this study comes from the special topology of the cell, overly complicated by the global geometry of the chamber. The response of the KLOE cell is primarily affected by its square shape and by the discrete cathodic edge.

The square cell shape entails a dependence of the time to distance relations on the angle ϕ that the particle trajectory makes with the y axis in the local cell reference frame (for the definition of angles and reference frame see inset in Fig. 1).

In the simplifying hypotheses of an "ideal" square cell, the time to distance relations, $r(t_d)$, depend on the track angle ϕ but must obey to the symmetries:

$$r(t_d;\phi) = r(t_d;-\phi) \tag{1}$$

$$r(t_d;\pi/4-\phi) = r(t_d;\pi/4+\phi). \tag{2}$$

Actually, the not constant position of the field wires at the outer cell boundary produce a deformation of the outer half of the drift area. As a consequence, the β_u angle affects the $r(t_d)$ function in a different way for each value of the track angle ϕ, thus spoiling the cell symmetry. The residual approximate symmetry one can still assume valid in the outer half cell is

$$r(t_d;\phi,\beta_u) = r(t_d;-\phi,-\beta_u) \tag{3}$$

while the symmetries in eq.1,2 hold in the lower half cell.

A second order effect in the cell response is due to the small difference between the values of the stereo angle of the sense wire and of field wires at the bottom side (of the order of one $mrad$) which produces a slight shift of the base of the cell, at the end plates, on the left or on the right side, according to the sign of the stereo angle. This deformation, parameterized by the angle β_l, increases monotonically (almost linearly) with z.

4.2 The analysis procedure: results for radial tracks

The time to distance relations have been obtained by using the prototype as a self tracking device (i.e., no external hodoscope was used). The track finding algorithm applied has been extensively described in ref. [9]. The impact parameter of the track in a given cell is measured by fitting all the remaining hits in the event to a straight track and by computing the distance of closest approach of the reconstructed track to the given sense wire. In order to get a first approximation of the track parameters, a very rough estimate of the time to distance relation has been used. The reconstructed tracks are, then, used for computing a more refined relation to be used as second order approximation. This quickly converging procedure (only two iterations are necessary) provides the time to distance relations.

Once the time to distance relation and the corresponding resolution function (see next section 4.4) are optimized for tracks crossing the detector radially ($\phi = 0$) in the plane $z = 0$, the asymmetries of the cell response can be exploited as a function of ϕ and β_u by means of 1.4×10^6 events recorded with the beam impinging on the detector in the transverse plane $z = 0$ and at different azimuthal angles.

4.3 The time to distance relations: $r(t_d)$

Fig. 3 shows the space to time relation obtained for radial tracks, or, equivalently, $\phi = 0^0$ and $\theta = 90°$, in $3 \times \pi$ cm^2 cells. In this configuration the β_u and β_l angles are expected not to affect the cell response, since, for every impact parameter of the track, the fastest drifting electrons are produced in a region of the cell far away from the corners. For this reason the space to time relation shown in fig. 3 has been obtained without selecting the hit cell according to the β_u and β_l values.

The functional dependence of the impact parameter on the measured time has been fit by means of three 4-th order polynomial branches: the first one covers the region of drift times from zero up to 450 ns, which correspond, in the distance domain, to impact parameters between zero and, roughly, one half of the half-cell width ($\sim$ 0.8 cm); the second one is joined to the first one by continuity and differentiability and is used for drift times in the range $450 \div 880$ ns (i.e. impact parameters up to ~ 1.4 cm); the last branch is connected by requiring only the function continuity at t=880 ns and it extends up to 1750 ns: this wide interval of drift times corresponds only to the last millimeter of the drift area. The increase of the electric field near the cathodic wires is responsible for the change in the sign of the second derivative of the time to distance relation which occurs at impact parameters $\sim 1.1 - 1.2$ cm. Then, the large spread of drift times in the last few millimeters of the cell is due to the very different drift paths travelled by the fastest electrons.

After the optimization of the space to time relation in fig. 3, we have verified that the hypothesis of independence of $r(t_d; \phi = 0°)$ from β_u was adequate (since the range of values of β_l is much smaller than that of β_u it can be safely neglected in this study). The use of data belonging to the *"fine z scanning"* allowed us to look for variations of the cell response within a z interval wider than a complete period of β_u. In fact, as discussed in ref. [10], the periodicity of β_u depends only on the value of the stereo angle ϵ and of the cell width. For KLOE, this periodicity is tipically of the order of $\sim$ 10 cm. The hits produced by radial tracks ($\phi = 0°, \theta = 90°$) in transverse planes with $| z |< 14$ cm were selected in nine samples according to the value of the β_u angle. Fig. 4 shows the space to time relation in the central bin, $| \beta_u |< 3.15°$, and the superimposition of the nine curves obtained in each slice. The negligible differences between the curves justify the obvious consideration that β_u, and furthermore β_l, are irrelevant for the cell response at $\phi = 0°$.

The dependence of the space to time relation on the angle ϕ was studied by using only hits falling in the lower half of the cell, where the almost uniform cell shape allows to disentangle the effect of the cell deformation parameterized by β_u. As expected, the time to distance relation turns out to be affected by ϕ only for impact parameters larger than $\sim$ 1 cm [1]. Therefore, the data have been fit with the same analytic expression for each value of ϕ and by constraining the parameters of the first branch and the first joining point to the values obtained in the $\phi = 0°$ case. By assuming the symmetries of eqs. 1 and 2, six intervals of ϕ angles have been set to reproduce the anysotropies of the cell response. The amplitudes of these intervals, listed in table 1, have been chosen in such a way to keep constant and roughly equal to the chamber resolution the average difference between one parameterization and those in the adjacent intervals. Fig. 5 shows the fit to the space to time relations in the six slices of ϕ, as defined in table 1.

[1]Here, as well as in the following, we refer, without loss of generality, to the $3 \times \pi$ cm^2 cells, where a slightly lower average drift velocity, 1.6 cm/μs compared to 2. 1 cm/μs in the smaller cells, enhances the edge and anisotropy effects.

ϕ interval no	$< \phi >$	$\Delta\phi$	$\sharp\beta_l$ intervals	$\sharp\beta_u$ intervals
1	$0°$	$10°$	1	1
2	$8.75°$	$7.5°$	2	3
3	$15°$	$5°$	2	5
4	$21.25°$	$7.5°$	2	5
5	$32.5°$	$15°$	2	5
6	$45°$	$10°$	2	7

Table 1: Definition of the ϕ intervals for the study of the time to distance relations. $< \phi >$ is the central value of the interval of width $\Delta\phi$.

A deeper investigation of the behaviour of the time to distance relations at large drift times and large track azimuthal angles pointed out the effect of the deformation of the cell shape in the inner-half cell, parametrized by β_l. Fig. 6 shows the correlation plot between drift times and impact parameters in the 6th slice of ϕ. The two different trends that can be recognized for $t_d > 1300$ ns are easily separated if one selects the hits according to the configuration of the cell in the lower half. Actually, in the prototype, the lower half of the cell is square not in the plane $z = 0$ (where the data used in this analysis were collected), like in the KLOE drift chamber, but on one end plate. Therefore, at $z = 0$, β_l acquires a value different from zero for every layer and of alternating signs from one layer to the following. The effect of the β_l angle increases with the track azimuthal angle and it entails, not only a difference in the $r(t_d)$ function but also a slightly different geometrical acceptance of the cell. Since the absolute value of β_l is quite small, no relevant discrepancies exist between different layers. Therefore, two time to distance relations, the first one for odd layers ($\beta_l < 0$) crossed at negative ϕ angles or even layers ($\beta_l > 0$) at $\phi \geq 0$ and the second one for the complementary cases, are enough to take into account this effect, which corresponds to what is going to happen near the end plates of the KLOE chamber. In the remaining region, obviously, a single parameterization ($\beta_l = 0$) will be sufficient. The parameterization of the space to time relations as a function of ϕ has been performed in the two cases $\beta_l \times \phi \geq 0$ and $\beta_l \times \phi \leq 0$ and the results are shown in fig. 7, where the fit to the time to distance relations for $t_d > 450$ ns are plotted.

A procedure of interpolation between the different functions applied after a first fit of the track, which allows to calculate the ϕ angle of the track in each local frame of the hit cells, has been shown to improve statistically the track reconstruction, by providing a more accurate conversion of the drift time.

After the optimization of the time to distance as a function of the track angle, the effects of the cell deformation at the outer cell boundary have been addressed in every ϕ interval. As already discussed, the cell response turns out to be independent from β_u when $\phi \sim 0$. As soon as the track angle in the cell becomes different from zero, a spread of the time to distance relations in the outer half of the cell appears as a consequence of the variations of the cell shape. This effect starts to be relevant for smaller values of the impact parameter when ϕ gets closer to 45^0. In order to disentangle the effects due to the β_u angle from those due to the track angle, only hits falling in the outer half of the cell have been used in every ϕ interval. The symmetry of eq. 3 has been verified and then assumed in the analysis of the data. For every value of ϕ, the hits have been grouped in equally spaced β_u slices. The width and the number of the β_u intervals in each ϕ bin, summarized in table 1, has been defined according to the overall spread of the time-to-distance correlation plots. Fig. 8 shows the space to time curves related to the different β_u slices in two ϕ slices where the cell deformation effect is large.

4.4 The resolution functions: $\sigma(t_d)$

The parameterization of the spatial resolution as a function of the measured drift time was performed following an iterative procedure similar to the one described in par. 4.3 for the determination of the time to distance relations. A first estimate of $\sigma(t_d)$ is used in the tracking program to obtain the track orientation in the cell and then, once the relevant track parameters are known, a more accurate parameterization is applied, which takes into account the dependence of σ on ϕ, β_l and β_u.

The resolution function is obtained from the distributions of the residues $\Delta r(t_d)$ between the drift distance assigned by the time to distance relation to the measured drift time in a given cell, and the impact parameter of the track in that cell, estimated by fitting all the remaining hits in the event to a straight line. These distributions have been plotted for slices of Δt, maximum width of 15 ns, and fitted to gaussians (see fig. 9) except in an interval of $\sim$ 1.25 mm around the sense wire. In this region, in fact, due to the low ionization statistics, the residues distributions exhibit a systematic overestimate and the resolution $\sigma(t_d)$ is computed by adding quadratically this offset to the r.m.s. of $\Delta r(t_d)$.

Firstly, the resolution was obtained for tracks crossing the detector normally in the plane $z = 0$ ($\phi = 0$), then for the different ϕ ranges in the two cases $\beta_l > 0$ and $\beta_l < 0$, by using only hits in the inner part of the cell and, finally, within each ϕ range, the effects of β_u were studied for hits belonging to the outer part of the cell. Different functions $\sigma(t_d, \phi, \beta_l, \beta_u)$ have been extracted from the data and fitted, to obtain an analytic parameterization of the resolution, with the following branches: 1) a rational function, 2) a 4-th order polynomial and, 3) for some values of ϕ and β_u, an exponential. The three branches are connected requiring function continuity.

Fig. 11 and fig. 12 show, respectively, $\sigma(t_d)$ in the case of tracks crossing the plane $z = 0$ at $\phi = 0$ in the cell reference frame, for the different ϕ ranges listed in par. 4.3 at $\beta_l > 0$ (a) and depending on the β_u interval for $40^\circ < \phi < 50^\circ$.

The branch 1) of the fitted functions describes the behaviour of the resolution in most part of the cell (up to $\sim$ 1.4 cm), reproducing well the large increase in the range of short drift times, where the contribution due to the ionization statistics dominates and the wide, almost constant minimum over a large range of impact parameter, in the region where the resolution is affected by the diffusion in the gas, by the time uncertainties of the electronics and by the interpolation error of the fitted track to the given cell. Finally, the sharp increase at $t_d > 700$ ns is due to the influence of the field wire at the edge of the cell. There, the drift velocity is slightly higher than in the middle of the drift area and, for a given impact parameter, the spread in the arrival time of the fastest electrons is increased. This second effect arises from the large difference in length among the electron drift trajectories departing from the field wire for tracks next to it and is amplified in helium because of the large mean free path for primary ionization. In fig. 13, where the drift trajectories and the isochronous are shown in the GARFIELD simulation of a typical Prototype 1 cell, this becomes clear by looking at the configuration of the drift lines close to the field wire, and will be further explained in section 5.

For larger impact parameters, the branch 2) describes the decrease of $\sigma(t_d)$, due to the fact that the fastest drift electrons come from the corner of the cell, where the drift velocity is low and the drift lines are all more radial.

Finally, the branch 3) is used only for those ϕ or β_u values for which the track orientation in the cell allows for longer drift trajectories and the resolution has a fast increase, due to the strong anisotropy of the electric field in that region.

5 A qualitative comparison with GARFIELD

In order to understand the cell response in terms of its geometrical configuration and of the transport phenomena in the gas mixture adopted, we have looked at the GARFIELD simulation of ionization electrons drifting in a cell of Prototype 1. We choose a cell of Prototype 1, cell # 9 of layer # 22, and the computation of the electric field inside the cell was reproduced by the program on the bases of a map of the relative positions, with respect to the sense wire of the selected cell, of 209 wires surrounding it. High voltages on sense wires and potentials on the guard wires were set to the values used during the data taking at the beam test. A description of the transport properties of the gas mixture, drift velocity and longitudinal diffusion, according to [11] was used as input, the distribution of the cluster size was taken from [12] and the number of primary ionizations in the gas was set to 16.7 cm^{-1} according to the result obtained with Prototype data [13] itself.

Drift lines and isochronous in the cell are plotted in fig. 13. In the same figure the dots superimposed to the cell map represent the sites of production of the clusters to which the fastest electrons belongs, for tracks crossing the cell at $\phi = -20°$. They have been obtained by finely sampling the cell area with tracks of $\phi = -20°$ and impact parameters between 0 and $w/(2cos\phi)$ ($w/2$ is the half cell width). For each track the whole process of ionization, drift and diffusion has been simulated and the drift time of the fastest electron, togheter with the x_{fe} and y_{fe} coordinates of the point (grey dots in fig. 13) of the track where it was produced, are recorded. The distribution of these points and of the drift line map clearly show that the anisotropy of the cell, mainly due to the discrete cathode (in the case of $\phi = -20°$ particularly relevant is the field wire at the left side of the cell), allows for drift paths geometrically disfavoured to be the fastest ones. Figg. 14 and 15 show a quite satisfactory agreement between the cell response observed in the data and the Monte Carlo: the knee of the time-to-distance relation occurs when the impact parameter becomes larger than $(w \cos \phi)/2$, i.e. when the track moves from the right to the left of the lateral field wire. This transition is due to the fact that, in the two cases, the first electrons come from regions of the cell completely separated.

As already pointed out, this situation strongly affect the trend of the resolution as a function of the drift time. Fig. 16 shows the resolution on the impact parameter obtained in the simulation of tracks of $\phi = -20°$ as a function of the distance of closest approach of the track to the sense wire. A steep increase of the resolution is observed, like in the data (see figg. 11 and 12), at impact parameters sligtly smaller than $(w \cos \phi)/2$ and, in general, every time the track gets close to a cathodic wire.

This situation is well illustrated in fig. 17 where the drift lines (and equal time contours) departing from a track at $\phi = 20°$ and impact parameter $d > w \cos \phi/2$ are shown (top plot) with the graph of the drift time as a function of the y coordinate of the point of the track from which a drift path has been simulated. The minimum drift time is almost independent on the cluster production site, since the drift time is very flat around the minimum, $y \sim 0.65$. Counterwise, when $d < w \cos \phi/2$ (bottom plot) the sharp minimum of the graph entails a large spread of the drift times induced by the dicrete nature of the ionization process. This explain the decrease of the resolution at drift times just above the time corresponding to $d = w \cos\phi/2$. Of course, the effect mush vanish at large ϕ angles and in fact, in the data, it is very small for $25^\circ < \phi < 40^\circ$ and it disappears when $40^\circ < \phi < 50^\circ$ (see fig.s 8 and 12). The time graphs in fig. 18 computed by GARFIELD for tracks at $\phi = -40^\circ$ for the two cases $d < w \cos\phi/2$ (top plot) and $d > w \cos\phi/2$ (bottom plot) show that in both situations the fastest paths are almost perpendicular to the track and the drift lines are parallel each other in this region, so that the minimum of the drift times is very broad.

6 Conclusions

A systematic study of the time to distance relations and the spatial resolutions, as a function of the track angle in the cell ϕ and of the cell deformations due to the stereo geometry (parametrized by the angles β_l and β_u), has been completed on the data collected at CERN with the Prototype 1 of the KLOE tracking chamber. The obtained spatial resolution is better than ~ 120 μm over a large part of the cell, independently of the angles described above.

References

[1] The KLOE Collaboration, The KLOE Central Drift Chamber, addendum to the KLOE technical proposal, LNF-94/028 (IR) (1994).

[2] F. Grancagnolo for the KLOE Collaboration, Full scale Prototype of the KLOE drift chamber, NIM A367 (1995) 108.

[3] M. Primavera for The KLOE Collaboration, NIM A379 (1996) 414.

[4] S. Spagnolo for the KLOE Chamber Group, Nucl. Phys. 54B (1997) 70; S. Spagnolo on behalf of the KLOE Tracking Group, "Results from the Full Length Prototype of the KLOE Drift Chamber", contribution to the "7th Pisa Meeting on Advanced Detectors", La Biodola, May 1997, to be published in NIM A.

[5] A. Andryakov et al., "The full length Prototype of the KLOE drift chamber", submitted to NIM A; A. Andryakov et al., KLOE memo # 103 (1997).

[6] R. Veenhof, GARFIELD a drift chamber simulation program - Version 3 (1991), CERN Program Library W5050.

[7] P. de Simone, KLOE memo # 35 (1995); P. de Simone, KLOE memo # 76 (1996).

[8] A. Andryakov et al., KLOE note # 115 (1994).

[9] G. Cataldi *et al.*, NIM A388 (1997) 127-134; M. Primavera, S. Spagnolo, KLOE note # 153 (1995).

[10] G. Finocchiaro, F. Grancagnolo and S. Spagnolo, KLOE note # 157 (1996).

[11] A. Sharma and F. Sauli, NIM A350 (1994) 470.

[12] H.Fischle *et al.*, NIM A301 (1991) 202.

[13] C. Luisi, KLOE memo # 78.

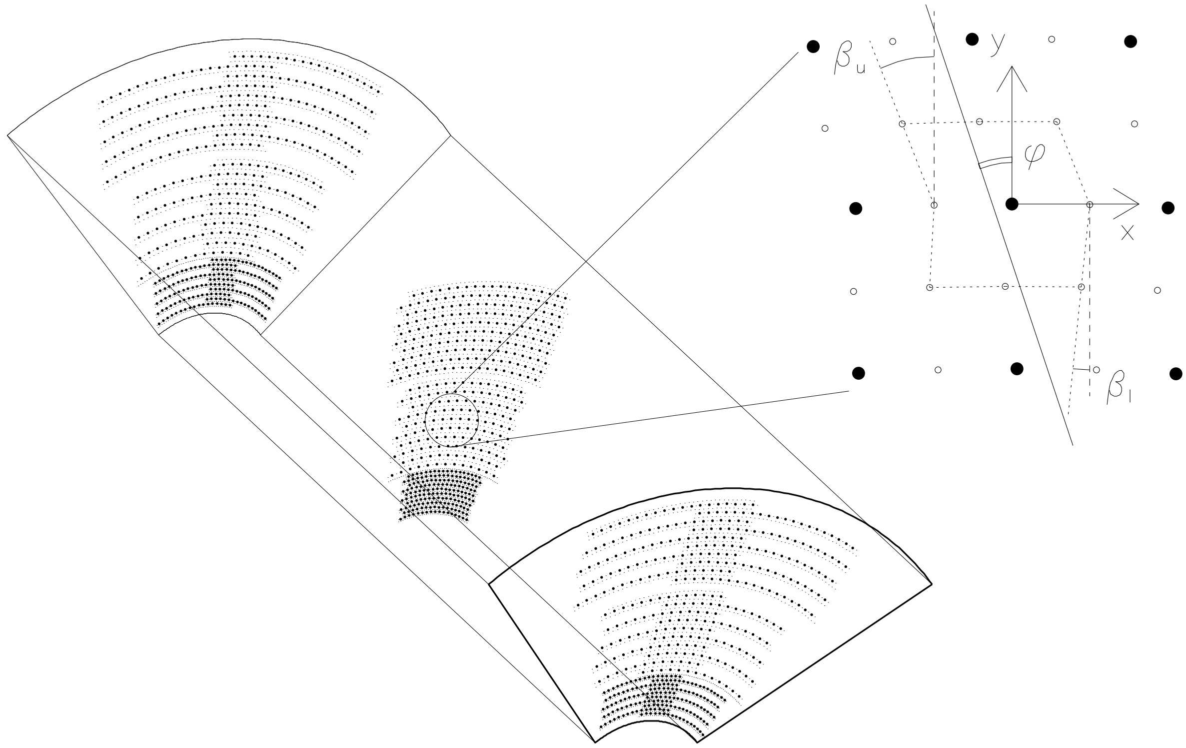

Figure 1: View of the prototype showing the position of the wires at the two end plates and at the center. The inset shows a cross section of a cell with the definition of the parameters ϕ, β_l and β_u.

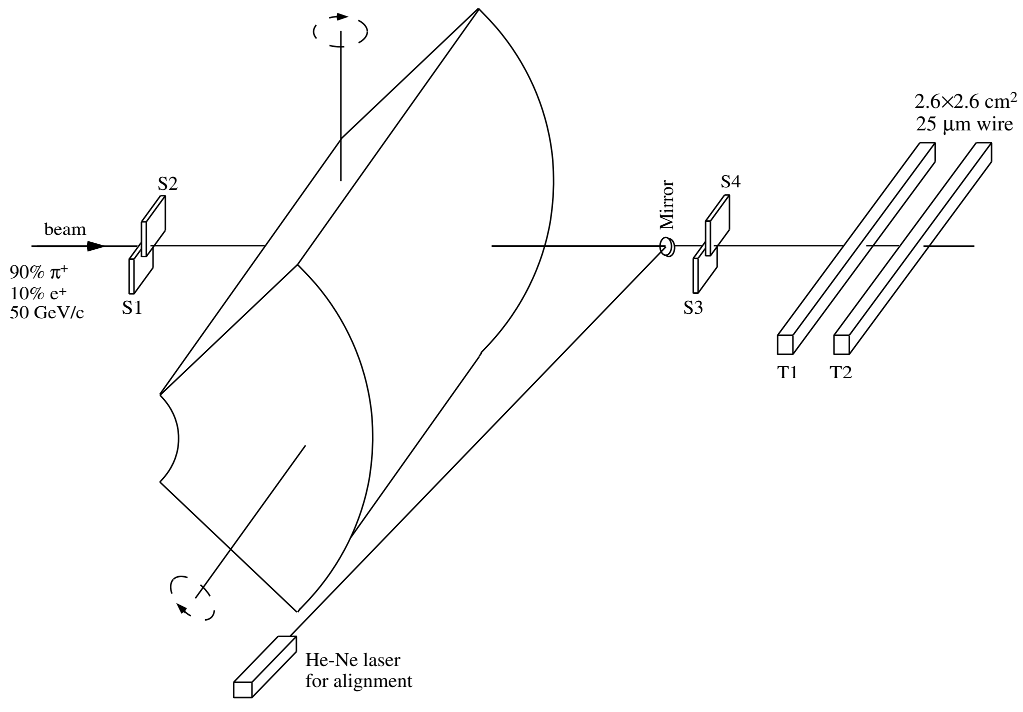

Figure 2: Schematic layout of the beam test.

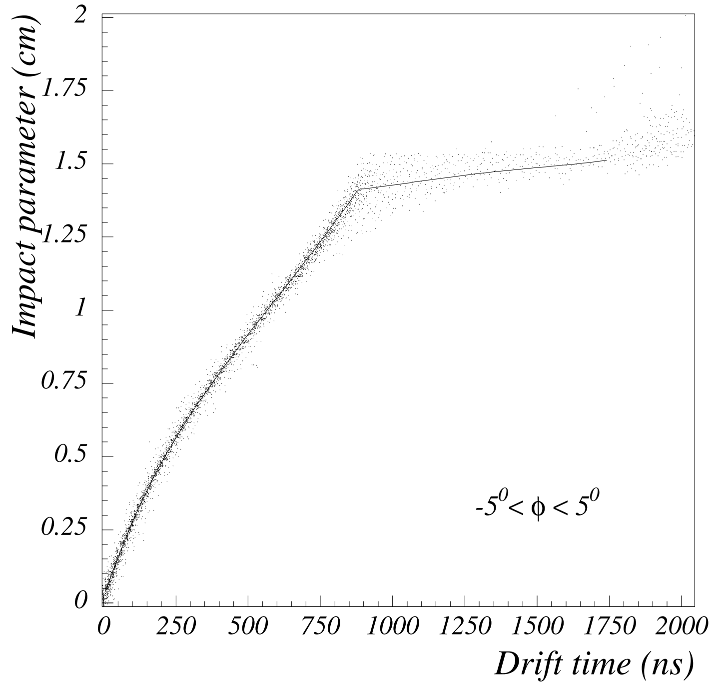

Figure 3: Scatter plot of the impact parameter versus the drift time for a $3 \times \pi$ cm^2 cell crossed radially ($\phi = 0°$). The fitting function described in the text is superimposed to the experimental points.

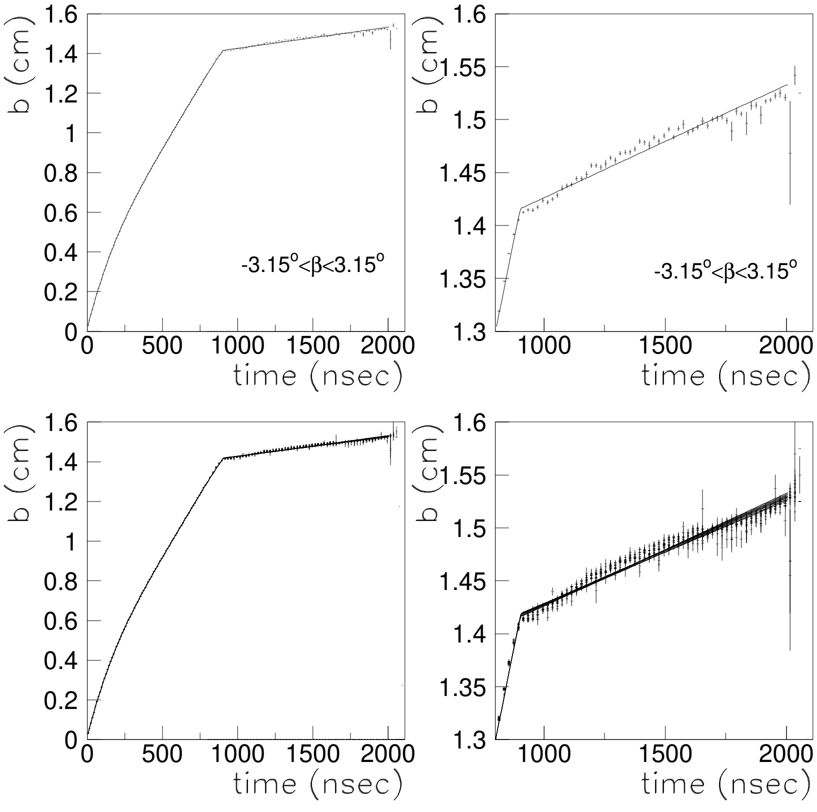

Figure 4: Time to distance relation for radial tracks, $\phi = 0°, \theta = 90°$, in a small interval of β_u (upper plots). In the lower plots the space to time relations obtained in nine intervals, 6.3° wide, of β_u are superimposed. On the right the region of large drift times is magnified.

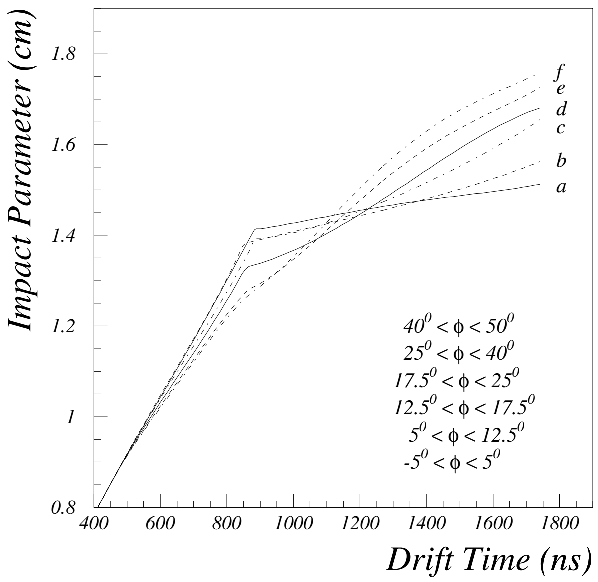

Figure 5: Impact parameters versus drift times for hits falling in the inner half of the cells in the $z = 0$ plane for different track orientations in the local reference frame. Only the region in which the cell anisotropy manifests itself is shown in the figure.

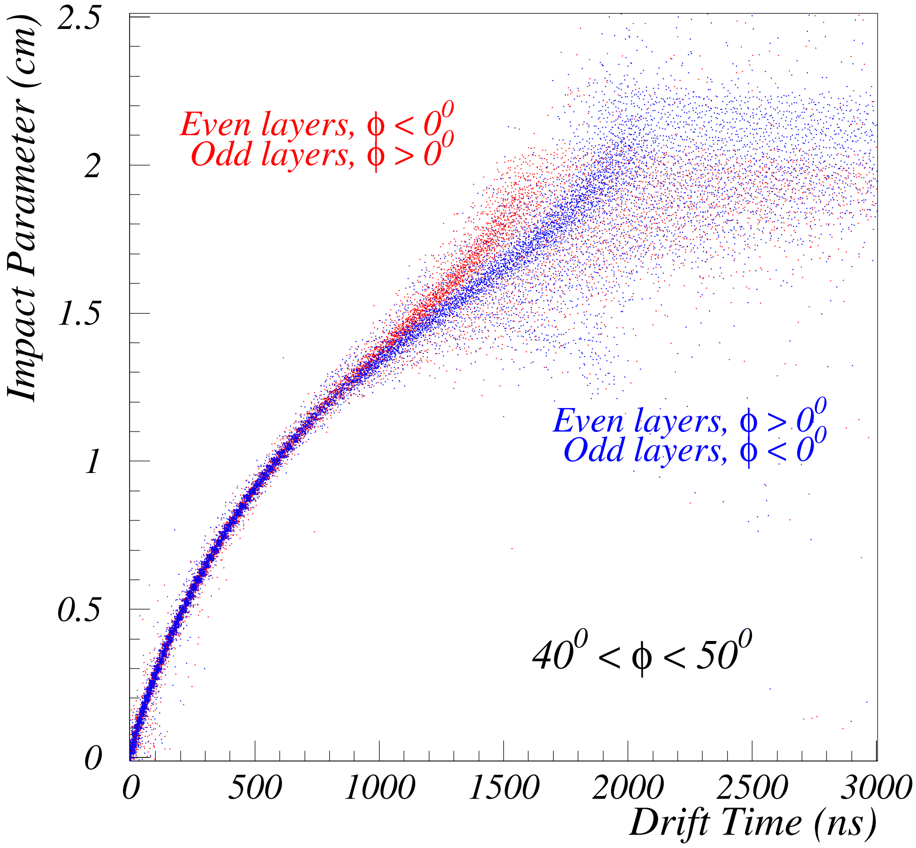

Figure 6: Impact parameters versus drift times for cells crossed in the $z = 0$ plane at $40^\circ < \phi < 50^\circ$ and in the lower half of the drift area. The two trends correspond to different deformations of the square shape of the lower-half of the cell, induced by the stereo configuration. The two cases can be distinguished by the sign of $\beta_l \times \phi$.

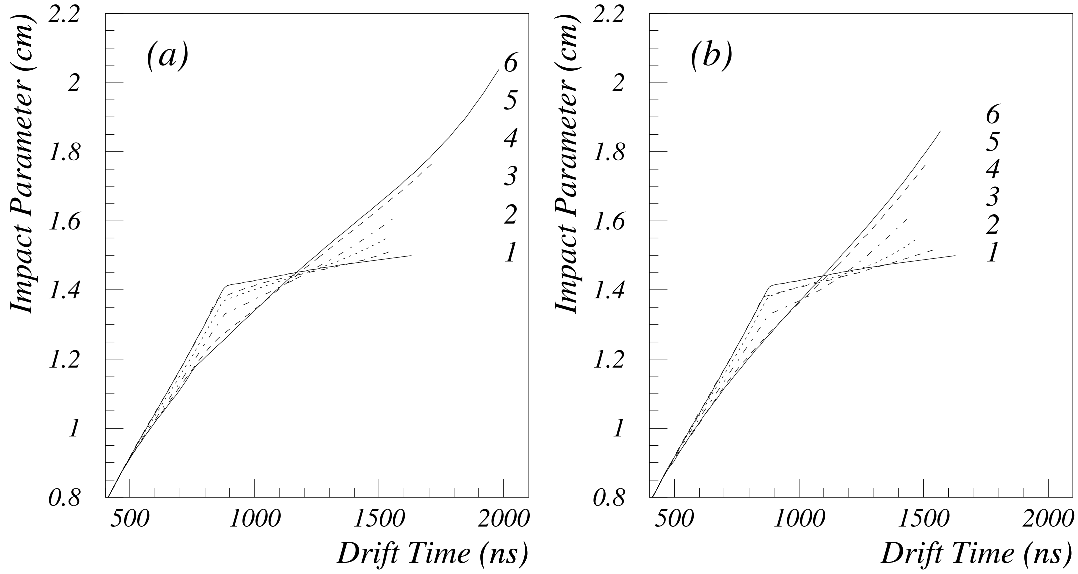

Figure 7: Time to distance relations for all the ϕ intervals. The plot (a) refers to odd layers crossed at negative ϕ angles and to even layers crossed at positive ϕ angles ($\beta_l \times \phi > 0$). The plot (b) refers to the hits with $\beta_l \times \phi < 0$. The numbering of the curves follows the convention defined in table 1.

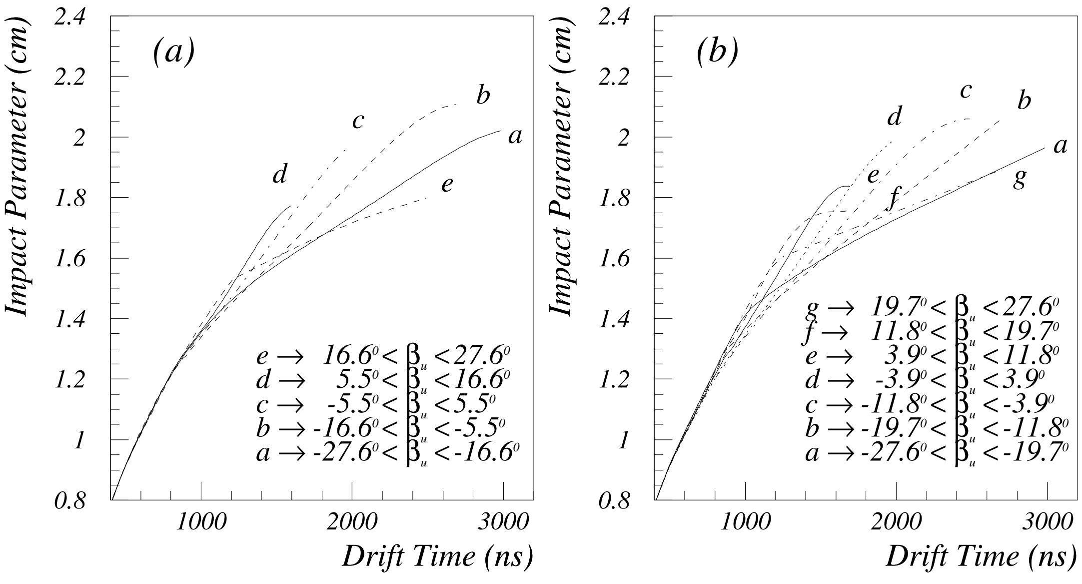

Figure 8: Time to distance relations for five intervals of the β_u angle in the case $25^\circ \leq \phi \leq 40^\circ$ (a) and for seven β_u slices in the case $40^\circ \leq \phi \leq 50^\circ$ (b).

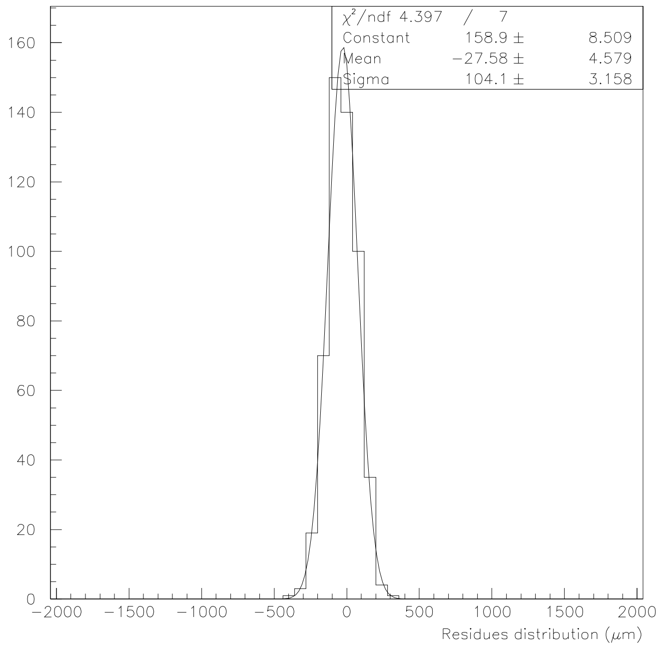

Figure 9: Distributions of the residues $\Delta r(t_d)$ (see text) for a drift time interval corresponding to ~ 10 ns at $r(t_d) \sim 5.6$ mm . A fit to a gaussian is superimposed.

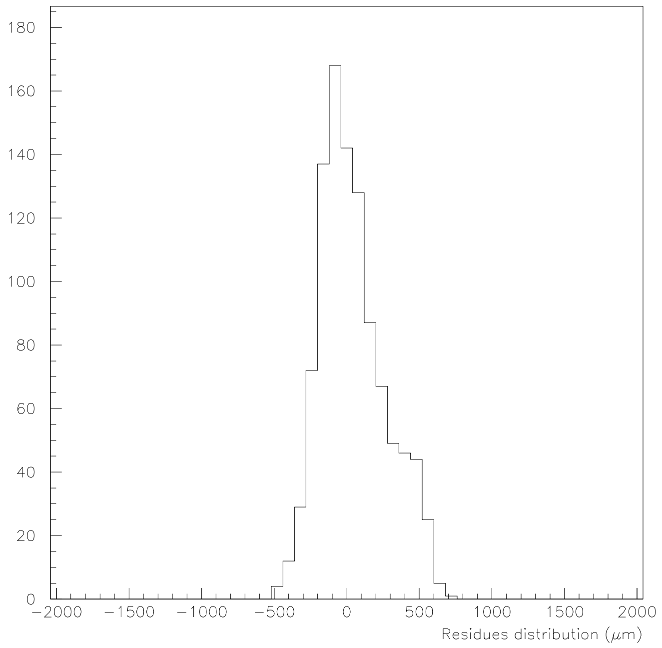

Figure 10: Not gaussian distributions of $\Delta r(t_d)$ for hits very close to the sense wire ($\sim 0.75 < r(t_d) <\sim 1$ mm).

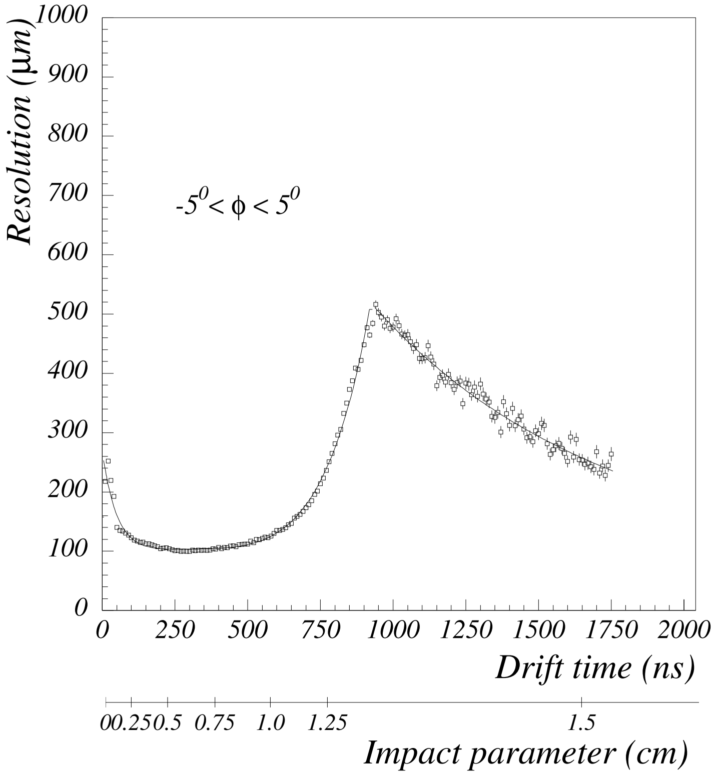

Figure 11: Resolution as a function of the drift time for $3 \times \pi$ cm^2 cells crossed radially ($\phi = 0°$). The fitting function superimposed to the points is described in the text.

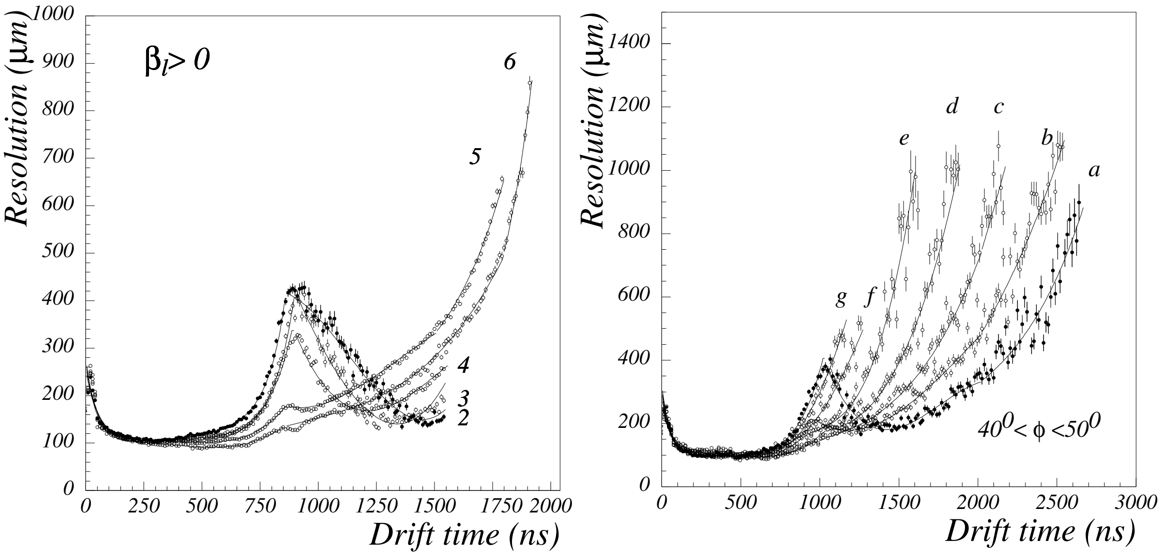

Figure 12: Resolutions as a function of the drift time in the five ϕ slices corresponding to not radial tracks (a), for hits falling in the inner half of cells with $\beta_l > 0$ (the curve labelling follows the convention in table 1). Resolution functions (b) in the outer half of the cell for $\phi = 45° \pm 5°$ and different value of the β_u angle describing the cell deformation at the top edge (here the labels attached to the curves refer to the same β_u intervals as in fig. 8b).

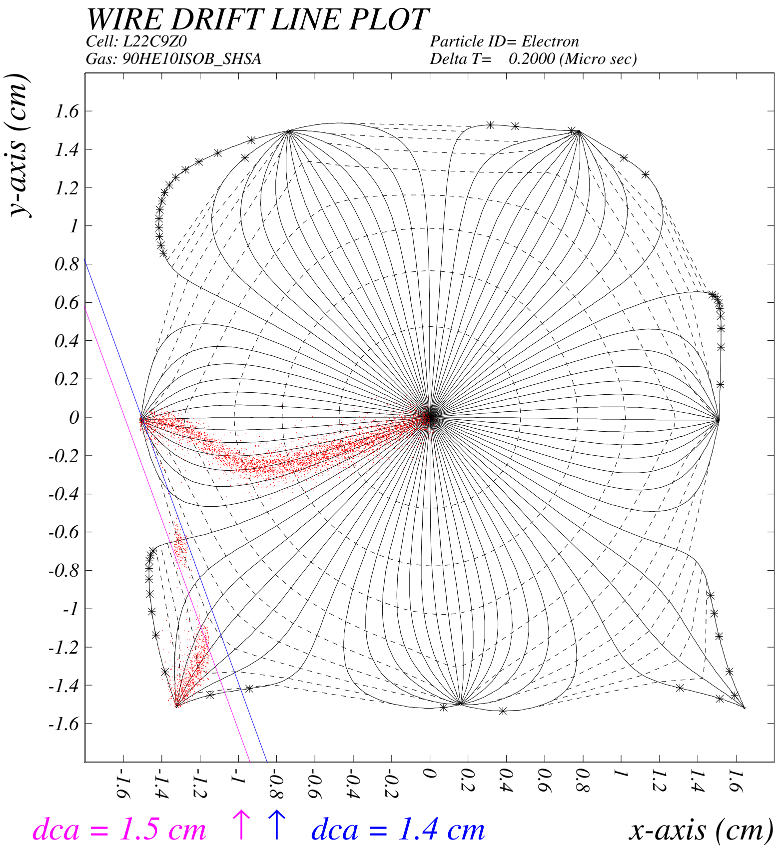

Figure 13: Drift lines and equal arrival time contours in the cell 9 of the 22-th layer of the drift chamber prototype at $z = 0$, as computed by GARFIELD. The gas mixture is 90% He 10% iC_4H_{10} and the HV on the sense wire is 1950 V. The dots superimposed represent the production sites, on tracks of azimuthal angle $\phi = -20°$, of the fastest electrons.

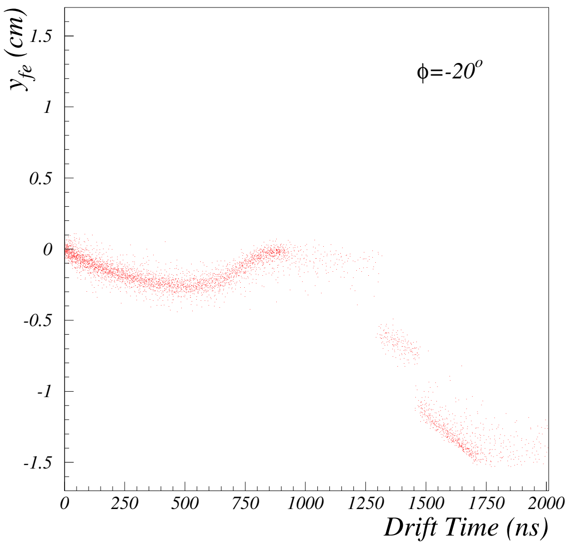

Figure 14: y_{fe} as a function of the drift time for the same simulated tracks as in fig. 13.

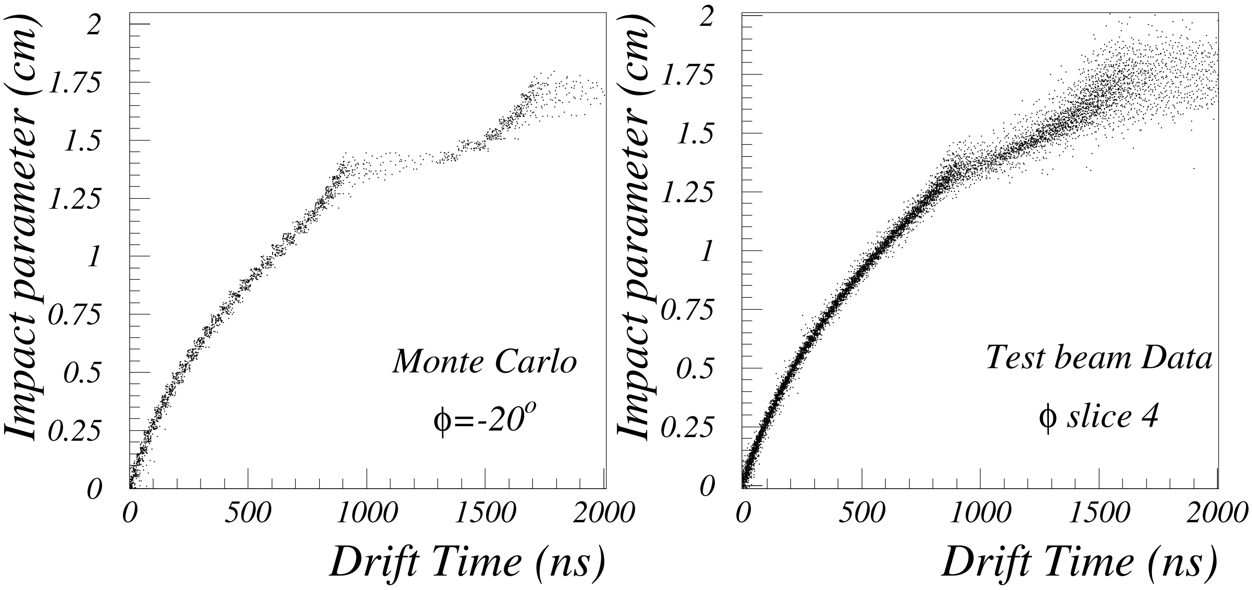

Figure 15: Comparison of the time-to-distance relation from simulated tracks crossing cell #9 of layer # 22 at $\phi = -20°$ and the time-to-distance relation obtained by looking at different cells of Prototype 1 crossed at ϕ angles in the range $17.5° \div 25°$ and $\beta_l \times \phi < 0$ (Note that negative ϕ tracks in cell #9 of layer # 22 correspond to $\beta_l \times \phi < 0$).

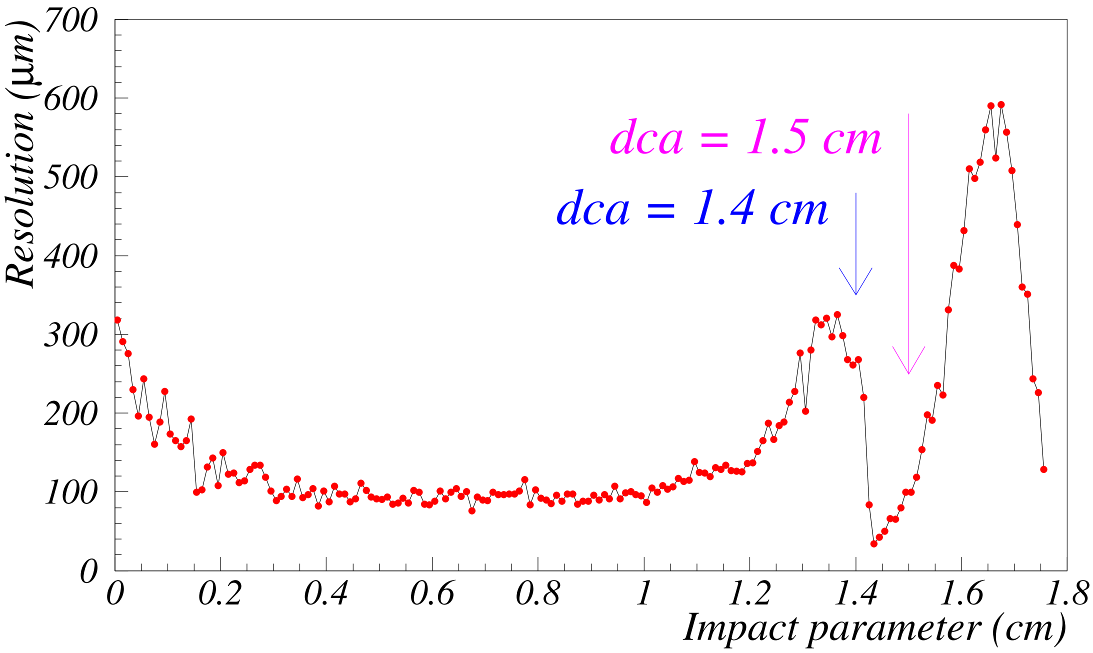

Figure 16: Resolution on the impact parameter obtained in the Monte Carlo for tracks at $\phi = -20°$. The only physical effects contributing to the resolution, which have been simulated, are the ionization statistics and the longitudinal diffusion.

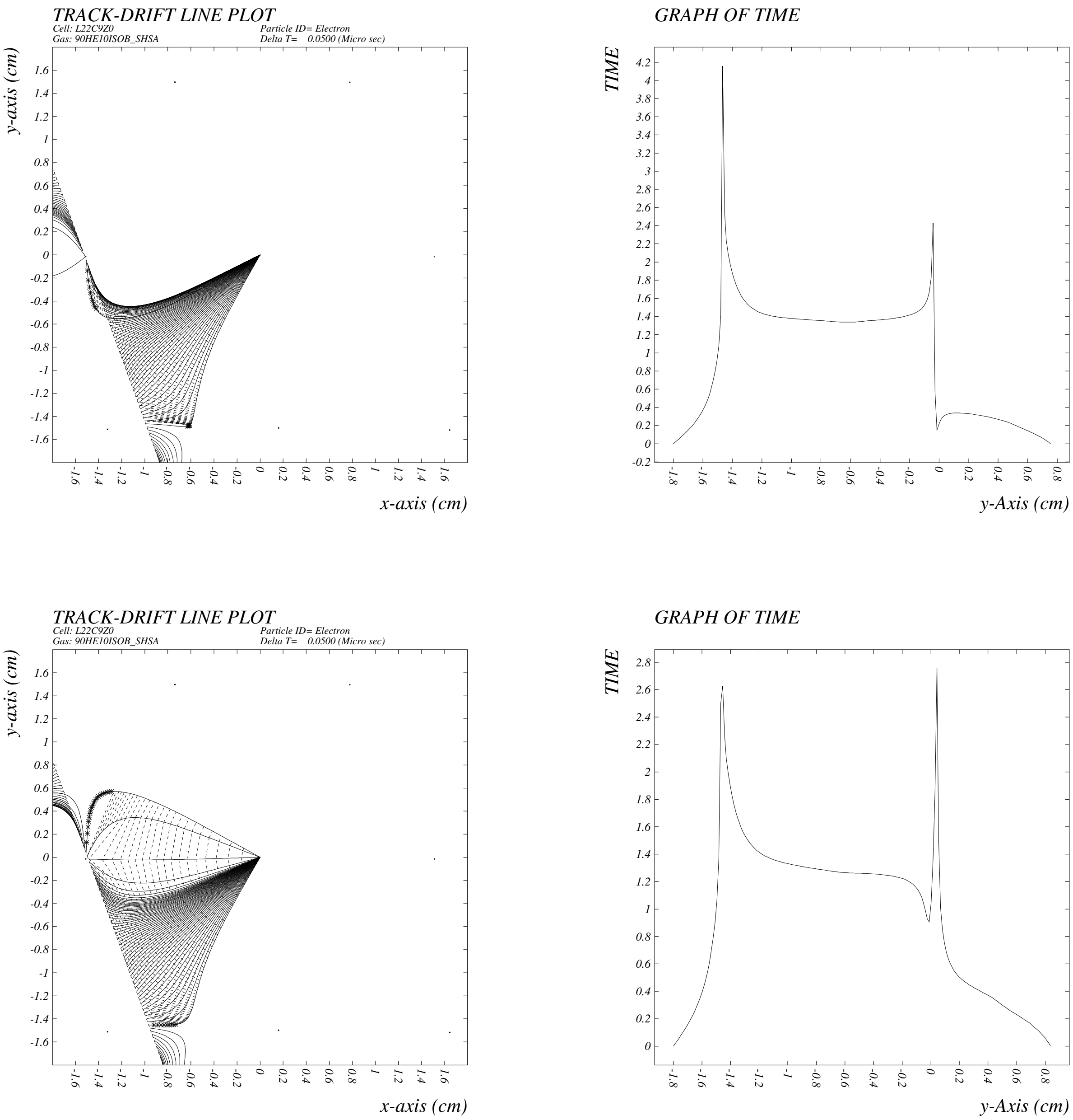

Figure 17: Drift lines departing from a track crossing cell # 9 of layer # 22 at $\phi = -20°$. The top-left plot refers to a track with impact parameter $d > w \cos \phi/2$, while the bottom-left to the opposite case. On the right the corresponding graphs of the drift time as a function of the y coordinate on the track are shown. Here only the region of the graph between the two maxima refers to electrons collected on the sense wire of the cell we are studying.

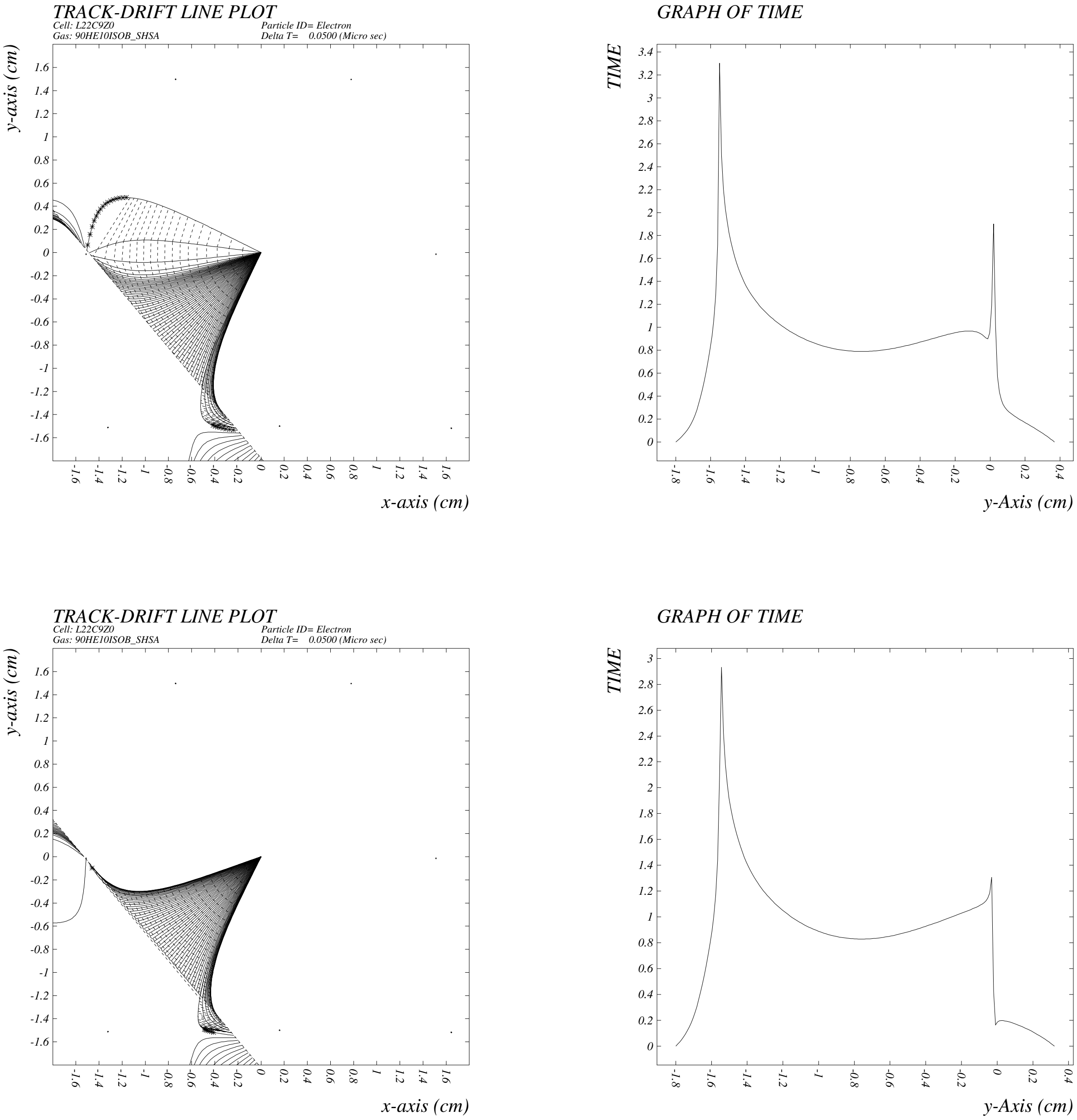

Figure 18: Drift lines departing from a track crossing cell # 9 of layer # 22 at $\phi = -40°$. The top-left plot refers to a track with impact parameter $d < w \cos\phi/2$, while the bottom-left to the opposite case. On the right the graphs of drift times as a function of the y coordinate on the track are plotted.